Geophys. J. Int. (2006) **166,** 529–542 doi: 10.1111/j.1365-246X.2006.03013.x

Electrical conductivity in the Earth's mantle inferred from CHAMP satellite measurements—I. Data processing and 1-D inversion

Jakub Velímský,[1,2] Zdeněk Martinec[1,3] and Mark E. Everett[2]

[1] *Department of Geophysics, Faculty of Mathematics and Physics, Charles University in Prague, Czech Republic. E-mail: jakub.velimsky@mff.cuni.cz*
[2] *Department of Geology and Geophysics, Texas A& M University, College Station, USA*
[3] *Section* 1.3, *GeoForschungsZentrum Potsdam, Germany*

Accepted 2006 March 17. Received 2006 February 14; in original form 2005 February 28

SUMMARY

A novel time-domain approach to the global electromagnetic induction problem is applied to vector magnetometer data observed by the CHAMP satellite. Data recorded during 11 storm events in 2001–2003 are processed track by track, yielding time-series of spherical harmonic coefficients. The data are then interpreted in terms of 1-D layered electrical conductivity models. The inversion is performed by full search of model parametric space which yields sensitivity of misfit with respect to conductivities of layers and positions of interfaces. In the upper 50 km the inversion solidly recovers a conductive layer corresponding to averaged surface conductance. The conductivity of the lower mantle is established at 6 S m^{-1} assuming the upper–lower mantle interface is fixed at the seismic-based 670 km boundary. However, the satellite data favour the models with a large jump around 1000 km to unrealistic conductivity values exceeding 10^3 S m^{-1}. The resolution of the method in the resistive upper mantle sandwiched between conductive crust and lower mantle is poor. Nevertheless, an upper bound of 0.01 S m^{-1} is suggested by the data. A conductivity increase in the transition zone is not observed.

Key words: electrical conductivity, electromagnetic induction, satellite observations.

1 INTRODUCTION

Studies of electrical conductivity of the crust and mantle by the electromagnetic (EM) induction method represent an important contribution to our knowledge of processes in the Earth's interior. Global and regional studies are traditionally based on long-term periodic variations observed at geomagnetic stations on the Earth's surface. The addition of geomagnetic field measurements from low-orbit satellites, such as MAGSAT, Ørsted, and CHAMP has provided a large improvement in terms of spatial coverage and motivated new research in this area. Olsen (1999) and, more recently, Constable & Constable (2004) inverted MAGSAT vector measurements in terms of 1-D conductivity. In the latter paper, a surface layer with conductance corresponding to global ocean was recovered. An upper conductivity bound of 0.01 S m^{-1} was suggested for the upper mantle. An increase of conductivity was not observed in the transition zone but occurs deeper, in the upper parts of the lower mantle, with a jump to 200 S m^{-1} at the depth of 1300 km.

Complicated spatiotemporal characteristics of satellite data favour the application of time-domain techniques for the global EM induction problem. Recently, this approach has been taken by Martinec *et al.* (2003) and Martinec & McCreadie (2004) in the case of earth with axially symmetric 2-D conductivity distribution, and by Hamano (2002), Velímský & Martinec (2005), and Kuvshinov *et al.* (2006) in the case of 3-D heterogeneous earth. Kuvshinov *et al.* (2006) applied an integral equation method to solve Maxwell's equations in the frequency domain and then obtained time-domain solutions by means of an inverse Fourier transform. Methods applied in the other papers are based on various integration schemes employed directly in the time domain.

Velímský *et al.* (2003) used the time-domain approach to estimate the response at satellite altitudes of a realistic heterogeneous mantle to storm-time excitation. They predicted anomalies of a few units of nT when compared to those induced by global 1-D models. Kuvshinov *et al.* (2006) studied the feasibility of 3-D inversion for the planned multisatellite SWARM mission. They concluded that a future three-satellite configuration will provide spatiotemporal coverage sufficient to detect large-scale conductivity anomalies deeply embedded in the mantle.

Here we present the first results of inversion of CHAMP vector magnetic data based on a time-domain forward method. The paper is organized as follows. In Section 2 we recall the time-domain method proposed by Martinec & McCreadie (2004) and discuss the assumptions for implementing this method. In Section 3 we give a detailed description of processing CHAMP magnetic vector data and apply the two-step, track-by-track spherical harmonic analysis. Inversion of CHAMP data in terms of 1-D conductivity models is presented in Section 4. Inversion in terms of a more complex, 2.5-D conductivity model (a 3-D model consisting of multiple 2-D segments with inverse problem solved

separately for each segment) is ongoing and will be reported in a future paper.

2 TIME-DOMAIN AXISYMMETRIC EM INDUCTION

The formulation of the EM induction problem appropriate for using low-orbit satellite observations is based on further development of the time-domain method first introduced by Martinec *et al.* (2003). It is a fast solver of the EM induction equation in a sphere with a 1-D layered or 2-D axially symmetric conductivity distribution excited by transient magnetospheric currents. Recently, the method has been modified by Martinec & McCreadie (2004). In particular, an insulating layer representing the atmosphere was included in the computational domain and a Dirichlet boundary condition was imposed on the horizontal component of the magnetic induction vector at satellite altitude. This reformulation is well suited for satellite data since one avoids the tricky problem of separation of the primary external and secondary induced internal fields. In this work, we improve the numerical implementation of the Martinec & McCreadie (2004) method. Sparsity of the linear algebraic system is fully exploited in the matrix assembly phase. The Gaussian elimination that was used originally is now replaced by LU factorization using the combined multifrontal/unifrontal method provided by the UMFPACK library (Davis & Duff 1999). The speed of the forward solver is increased approximately tenfold. A time integration over 2987 CHAMP tracks with 1 hr time step, 108 radial layers, and spherical harmonic truncation degree 8 takes less than 5 s on a 2 GHz Pentium 4 PC.

The forward method is based on a decomposition of the toroidal vector magnetic potential into spherical harmonic functions. The outer boundary condition is prescribed by the time-series of the spherical harmonic coefficients $\{X_j^i = X_j(t_i)\}$ of the horizontal northward component X of the total field (sum of primary and induced),

$$X(b, \vartheta; t_i) = \sum_{j=1}^{\infty} X_j^i \frac{\partial Y_j(\vartheta)}{\partial \vartheta}, \tag{1}$$

where b is the radius of the outer boundary of the insulating layer, that is, the average radial distance of the satellite over the duration of the storm, j is the spherical harmonic degree,

$$Y_j(\vartheta) = P_j(\cos\vartheta) \tag{2}$$

are zonal spherical harmonics, and P_j are fully normalized Legendre polynomials. The vertical component Z is predicted by the forward routine for a given conductivity model and compared with satellite observations. In terms of spherical harmonic coefficients,

$$Z(b, \vartheta; t_i) = \sum_{j=1}^{\infty} Z_j^i Y_j(\vartheta). \tag{3}$$

In this paper we assume that:

(i) electrical conductivity varies only radially;
(ii) ring-current excitation has an axially symmetric geometry;
(iii) satellite flies on a nearly polar orbit;
(iv) satellite moves sufficiently fast compared to the time variations of the ring current.

The first two assumptions are traditionally used in ground-station-based (e.g. Olsen 1998) and satellite-based (Constable & Constable 2004) studies. Although the key point of satellite induction research is to study lateral conductivity heterogeneities in the Earth and although the second assumption has been challenged recently (Balasis *et al.* 2004; Olsen & Kuvshinov 2004), (i) and (ii) are still useful when implementing a new, time-domain technique. Assumption (ii) also rules out the use of this technique for EM induction powered by daily variations of ionospheric currents due to their day-side night-side dichotomy. Moreover, since the satellite measurements take place above the ionosphere it is not possible to distinguish primary ionospheric currents and their induced counterparts from satellite data only.

Assumptions (iii) and (iv) allow us to separate in a simple way the spatial and time changes of the geomagnetic field observed by a single satellite. Each night-side satellite track is considered to sample a snapshot of the axisymmetric magnetic field at time t_i, that is, when the satellite crosses the equator. A spherical harmonic analysis of each track is then performed separately. The original intent of this study was to use vector magnetic data recorded by

Table 1. Geomagnetic storms from years 2001–2003 and CHAMP tracks used in this study.

Storm	Days			CHAMP night-side tracks					
	From	To	Total	First[a]	Last[a]	Total	Missing[b]	Dir.	Rev.[a]
1	2001/09/21	2001/10/07	17	6669	6931	263	0	Asc.	7
2	2001/10/11	2001/10/27	17	6978	7240	262	1	Asc.	7
3	2001/11/17	2001/11/29	13	7550	7751	197	5	Desc.	6
4	2002/04/07	2002/04/26	20	9738	10 047	306	4	Asc.	7
5	2002/08/24	2002/09/12	20	11 897	12 207	311	0	Desc.	5
6	2002/09/22	2002/10/12	21	12 348	12 673	324	2	Desc.	4[c]
7	2003/05/18	2003/06/01	15	16 048	16 280	233	0	Desc.	3
8	2003/06/07	2003/06/21	15	16 359	16 591	233	2	Desc.	3
9	2003/07/01	2003/07/24	24	16 732	17 105	374	1	Desc.	3[d]
10	2003/10/19	2003/11/03	16	18 445	18 694	250	12	Asc.	3
11	2003/11/11	2003/11/25	15	18 804	19 037	234	6	Asc.	5
Total			193			2 987	33		
Q[e]	2003/10/06	2003/10/12	7	18 244	18 352	109	8	Asc.	3

[a]Track (orbit) numbers and data revision versions as provided by *CHAMP Information System and Data Center* (see text).
[b]Tracks dropped from the analysis because of large gaps in measurements or no data.
[c]For days between 2002/09/22 and 2002/09/26 revision 5 was used.
[d]For days between 2003/07/01 and 2003/07/18 revision 1 was used.
[e]Additional 'event' consisting of seven quiet days and processed in the same way as the geomagnetic storms.

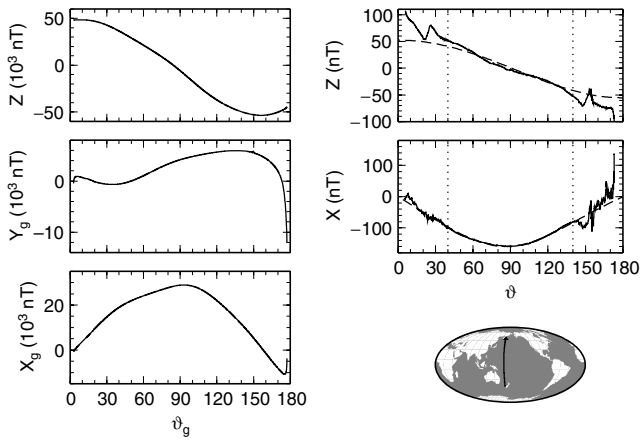

Figure 1. CHAMP satellite data from track 18 968 (arrow on global map insert), which samples the relaxation phase of storm 11 above the Pacific Ocean. Left plates: The original CHAMP data plotted along geographic colatitude ϑ_g. X_g, Y_g and Z components point, respectively, to the geographic north, east and downwards. Right plates: Solid lines denote the CHAMP (X, Z) data after removal of the comprehensive model, rotation into dipole coordinates and removal of a constant shift from the Z component. Dashed lines show the results of the two-step spherical harmonic analysis, including the extrapolation in the polar areas. For this particular track we use data from the colatitude interval (40°, 140°), as marked by dotted lines.

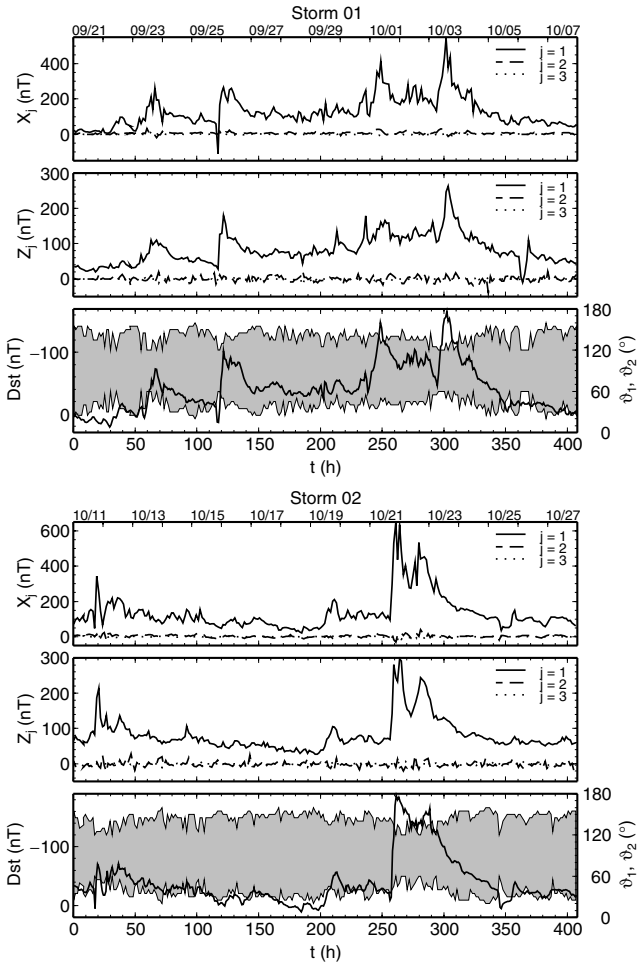

Figure 2. Time-series of spherical harmonic coefficients X_j^i and Z_j^i of horizontal and vertical components obtained by the track-by-track analysis of CHAMP data for 11 selected storms and the quiet interval Q. Only coefficients for degrees 1, 2, and 3 are shown with solid, dashed, and dotted lines, respectively. Time on the horizontal axis is measured from midnight (GMT) of the first day of each series (see Table 1). The *Dst* index is shown by solid lines in the bottom plots for each storm. The grey shadowing shows the colatitude interval used in the spherical harmonic analysis for each track.

both CHAMP and Ørsted satellites. However, Ørsted's inclination of 96.1° deviates considerably from the polar orbit. Forward EM induction modelling tests comparing the presented 2-D approach with full 3-D time-domain simulations (Velímský & Martinec 2005) showed that Ørsted's orbit is not suitable for the simplified 2-D axisymmetric approach based on assumption (iii). Therefore, we limit our efforts to processing data provided by CHAMP.

3 CHAMP DATA ANALYSIS

3.1 Selection and processing of vector data

The data analysed in this study were recorded by the vector flux gate magnetometer on board CHAMP. The satellite was launched on July 15, 2000 into a near polar orbit (inclination 87.3°) with initial altitude 454 km. Since the electromotive force acting on charged particles in the mantle is proportional to $\partial \mathbf{B}/\partial t$ we concentrate on storm-time data. Rapid increase of magnetospheric ring current in the initial phase of the storm followed by approximately exponential decay (Everett & Martinec 2003) results in strong electrical currents induced deep in the Earth's mantle which are sensitive to conductivity distribution.

Since the right ascension of the satellite moves slowly with respect to the Sun, the satellite's local time is different for different storms. In order to minimize the effect of strong day-side ionospheric currents we use only night-side data recorded by the satellite between 19:00 and 7:00 local solar time. From all records spanning more than 4 yr we have selected 11 events, each of 13–24 days in duration. Judging from the *Dst* index, these events cover the time intervals when the geomagnetic field was significantly disturbed by geomagnetic storms and CHAMP records from suitable local times were available. The night-side tracks are either ascending or descending, but not both during any given storm. An overview of the storms and corresponding CHAMP data is summarized in Table 1. Additionally, we have selected an interval of seven quiet days ($|Dst| < 35$ nT) from October 2003 to act as a control for the study.

We use various revision versions of data provided by the *CHAMP Information System and Data Center*.[1] Differences in the results of the spherical harmonic analysis applied to different data revisions for the same storm are negligible. Nevertheless, with the exception of storms 6 and 9, we always use the latest available revision consistently for the whole event.

In the first stage of data processing we filter out incomplete tracks with data gaps larger than 2° in colatitude. In the next step we use the comprehensive model of the Earth's magnetic field (Sabaka *et al.* 2002, 2004) to isolate signals corresponding to induction by storm-time magnetospheric currents. Using the version CM3e-K_3 (also denoted as CM4) of the comprehensive model we remove from the CHAMP magnetic data:

(i) main and crustal fields and secular variation up to degree 65;

[1] `http://isdc.gfz-potsdam.de/champ/`

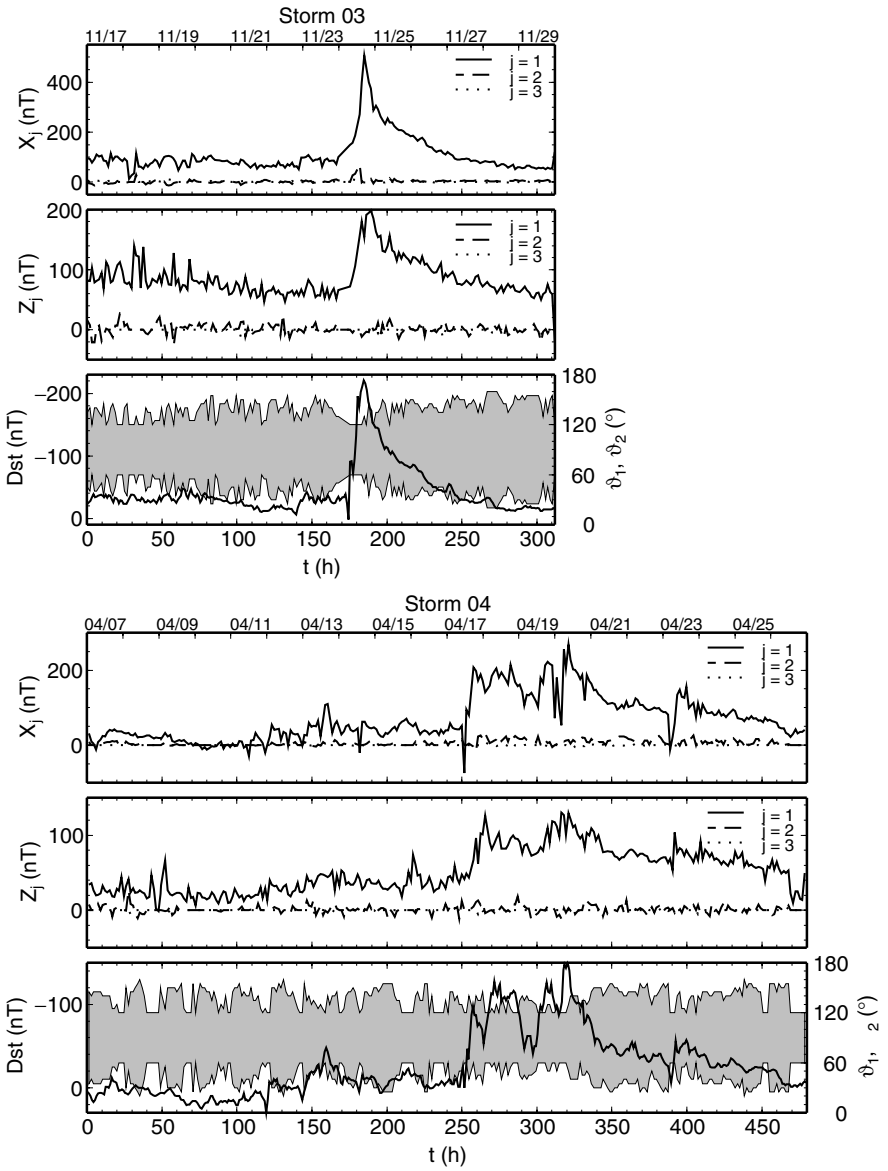

Figure 2. (*Continued*.)

(ii) field of ionospheric currents and corresponding induced currents;

(iii) model of toroidal field.

Note that the contribution of ionospheric currents (ii) is much smaller on the night side than on the day side. The toroidal field (iii) corresponds to radial electric currents connecting the ionosphere with magnetosphere. In the comprehensive model it is modelled using *in situ* vector observation by the Ørsted satellite.

Horizontal magnetic components (X, Y) are then rotated from geographic coordinates to dipole coordinates, assuming that the dipole axis intersects the Earth's surface at (78.8°N, 70.7°W). Since we assume axisymmetric geometry of external currents and only depth-dependent conductivity, the component in the direction of dipolar longitude is not considered further and henceforward we use X and Z to describe, respectively, the northward and downward magnetic components in dipolar coordinates. Finally, we shift the Z component at each track by a constant so that $Z = 0$ at the dipolar equator. The constant shift corresponds to zero degree spherical harmonic which cannot be predicted by forward modelling from the horizontal component. Fig. 1 shows an example of original and processed data from CHAMP track No. 18 968.

3.2 Spherical harmonic analysis

The two-step track-by-track spherical harmonic analysis proposed by Martinec & McCreadie (2004) is applied to both the CHAMP vertical and horizontal components. This method allows us to ignore measurements from the polar regions which are contaminated by signals from field aligned currents and polar electrojets. Instead, the field in these regions is extrapolated from the field at low and mid-latitudes in accordance with the assumption that global EM induction is driven by the equatorial ring current.

Let us assume that uncontaminated data for the ith track span the colatitude interval $(\vartheta_1^i, \vartheta_2^i)$. Using the linear transformation

$$\vartheta'(\vartheta) = \frac{\vartheta - \vartheta_1^i}{\vartheta_2^i - \vartheta_1^i}\, 180^\circ, \tag{4}$$

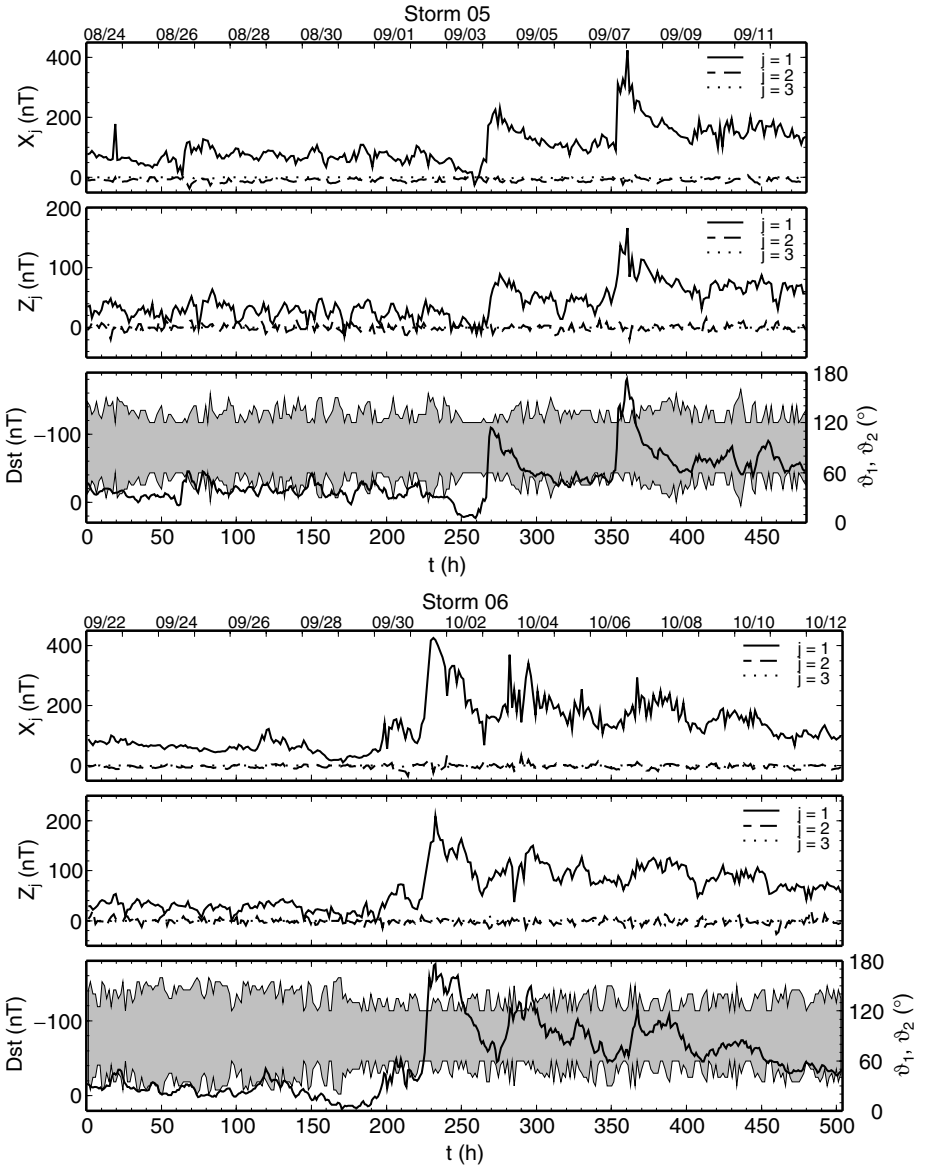

Figure 2. (*Continued*.)

which maps the interval $(\vartheta_1^i, \vartheta_2^i)$ onto the half-circle $(0, 180^\circ)$, we can expand both the horizontal and vertical component into spherical harmonic series,

$$X^i(\vartheta') = \sum_{j=0}^{N'} {X'}_j^i \, Y_j(\vartheta'), \tag{5}$$

$$Z^i(\vartheta') = \sum_{j=0}^{N'} {Z'}_j^i \, Y_j(\vartheta'). \tag{6}$$

The series are truncated at $N' = 25$ a sufficiently large degree to fit small-scale features in the data. The coefficients of the expansion are determined using a least-squares method. In addition, we implement a simple method to remove outliers. If any data point differs from the least-squares fit by more than 10 nT it is dropped and the least-squares fit is repeated until no outliers are indicated.

In the second step of the analysis, we find the coefficients X_j^i and Z_j^i by solving the equations

$$\frac{2\pi^2}{180^\circ} \sum_{j=1}^{N_X^i} X_j^i \int_{\vartheta'=0^\circ}^{180^\circ} \left. \frac{\partial Y_j(\vartheta)}{\partial \vartheta} \right|_{\vartheta(\vartheta')} Y_k(\vartheta') \, \sin\vartheta' \, d\vartheta' = {X'}_k^i, \tag{7}$$

$$\frac{2\pi^2}{180^\circ} \sum_{j=1}^{N_Z^i} Z_j^i \int_{\vartheta'=0^\circ}^{180^\circ} Y_j\left(\vartheta(\vartheta')\right) \, Y_k(\vartheta') \, \sin\vartheta' \, d\vartheta' = {Z'}_k^i, \tag{8}$$

for $k = 0, 1, \ldots, N'$. By $\vartheta = \vartheta(\vartheta')$ we denote inverse mapping to (4). The choice $N_X^i, N_Z^i < N'$ implies that both systems of linear eqs (7) and (8) are overdetermined and are solved by a least-squares method. Respective substitutions of coefficients X_j^i and Z_j^i into eqs (1) and (3) yield smooth approximations of X and Z components inside the colatitude interval $(\vartheta_1^i, \vartheta_2^i)$ as well as undisturbed extrapolations into the polar areas $(0^\circ, \vartheta_1^i) \cup (\vartheta_2^i, 180^\circ)$.

The crucial points in the method are (i) the selection of the truncation degrees N_X^i, N_Z^i and (ii) the determination of the interval $(\vartheta_1^i,$

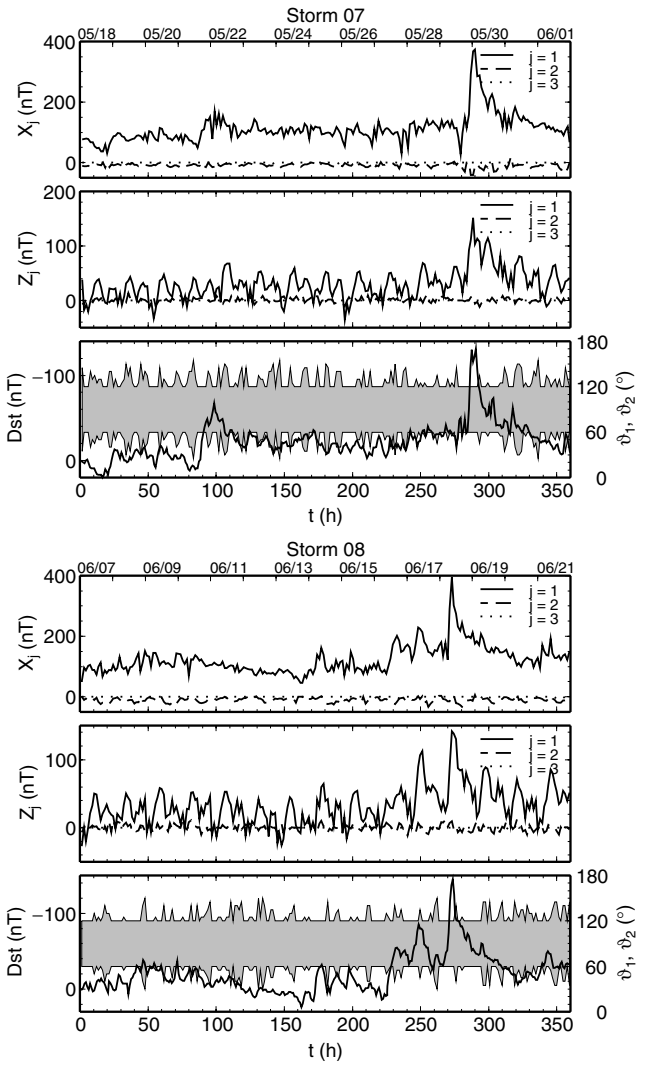

Figure 2. (*Continued*.)

ϑ^i_2) where data are free of the polar disturbances. These parameters are found for each track individually by the following scheme. We start with a broad colatitude interval $(\vartheta^i_1, \vartheta^i_2) = (20^\circ, 160^\circ)$. The truncation degree N^i_X is initially set to 2 and then increased gradually as long as the following conditions are satisfied: (i) the degree power spectrum is monotonically decreasing with increasing degree j:

$$j\,(j+1)\left(X^i_j\right)^2 \le (j+1)\,(j+2)\left(X^i_{j+1}\right)^2, \tag{9}$$

for all $j = 1, \ldots, N^i_X - 1$, and (ii) the harmonic extrapolation of $X^i(\vartheta)$ is, respectively, decreasing and increasing at the southern and northern pole, that is,

$$\sum_{j=1}^{N^i_X} X^i_j \left.\frac{\partial^2 Y_j}{\partial \vartheta^2}\right|_{\vartheta=0^\circ} \le 0, \tag{10}$$

$$\sum_{j=1}^{N^i_X} X^i_j \left.\frac{\partial^2 Y_j}{\partial \vartheta^2}\right|_{\vartheta=180^\circ} \ge 0. \tag{11}$$

The first condition is based on the assumption that the power of the magnetic field from the external ring currents is concentrated in low-degree terms, especially in the $j = 1$ term and the leaking of EM energy into higher degrees caused by the Earth's conductivity heterogeneities is small. The second condition excludes unrealistic oscillatory behaviour of the X component in the polar regions caused by a high-degree extrapolation. Once any of these conditions is violated, we fall back to the previous N^i_X and stop the iteration.

In the next step we compare the least-square approximation of $X^i(\vartheta)$ with the satellite data for colatitudes close to the boundaries of the interval $(\vartheta^i_1, \vartheta^i_2)$. If any data point in $(\vartheta^i_1, \vartheta^i_1 + 5^\circ) \cup (\vartheta^i_2 - 5^\circ, \vartheta^i_2)$ differs from the least-square approximation by more than 10 nT, we assume that the contamination of mid-latitude magnetic field by polar currents is considerably large. The colatitude interval is narrowed by 5° on both ends and the analysis is repeated with new values of ϑ^i_1 and ϑ^i_2. A suitable N^i_X has to be found again for the modified interval. This process is stopped when there is good agreement between the satellite data and the least-square approximation at the boundaries of the interval, as described above, or when $(\vartheta^i_1, \vartheta^i_2)$ reaches $(60^\circ, 120^\circ)$. Note that the colatitude interval is always symmetric with respect to the equator.

The colatitude interval could be also selected manually. However, this quantitative algorithm allows automatic processing of large number of tracks and was visually checked for randomly selected tracks.

The harmonic analysis of the vertical component $Z^i(\vartheta)$ is performed using the same colatitude interval determined for the horizontal component $X^i(\vartheta)$. The truncation degree N^i_Z is chosen such that: (i) the degree power spectrum decreases with increasing degree, that is,

$$\left(Z^i_j\right)^2 \le \left(Z^i_{j+1}\right)^2, \tag{12}$$

for all $j = 1, \ldots, N^i_Z - 1$, and (ii),

$$N^i_Z \le N^i_X. \tag{13}$$

The procedure applied to all track data for storms 1–11 results in the time-series of spherical harmonic coefficients X^i_j and Z^i_j. The coefficients from the missing tracks are filled in by cubic spline interpolation. The results are summarized in Fig. 2, where the first three harmonic coefficients for both components are plotted as functions of time after onset of magnetic storm. As expected, there is a high correlation between the first-degree harmonics X^i_1 and Z^i_1 and the *Dst* index. Moreover, the colatitude interval $(\vartheta^i_1, \vartheta^i_2)$ for each track used in the analysis is also shown. Note that during the peak activity of the storms, the interval narrows as polar current disturbances extend equatorwards to mid-latitude regions. The actual truncation degrees N^i_X and N^i_Z vary, respectively, between 1–7 and 1–4 with mean values 2.60 and 2.02.

3.3 Spectral analysis

Although our method is based on the time-domain approach it is useful to check the spectra of the X^i_j and Z^i_j time-series. First two plates in Fig. 3 show the power spectra estimates of first three spherical harmonic coefficients of vertical and horizontal field corresponding to Storm 1. Maximum entropy (ME) method (Press *et al.* 1992) is used to evaluate the spectra. Since we use finite-length time-series the spectra have infinite support. The power of first-degree coefficients corresponding to frequency 1 cpd is about two orders of magnitude smaller than the maximum in the low-frequency range and only slowly decreases for higher frequencies. That yields a difference of about one order in the magnetic field amplitudes. In the frequency domain analogy the waves at frequencies above 1 cpd correspond to penetration depths in the upper mantle. Despite of

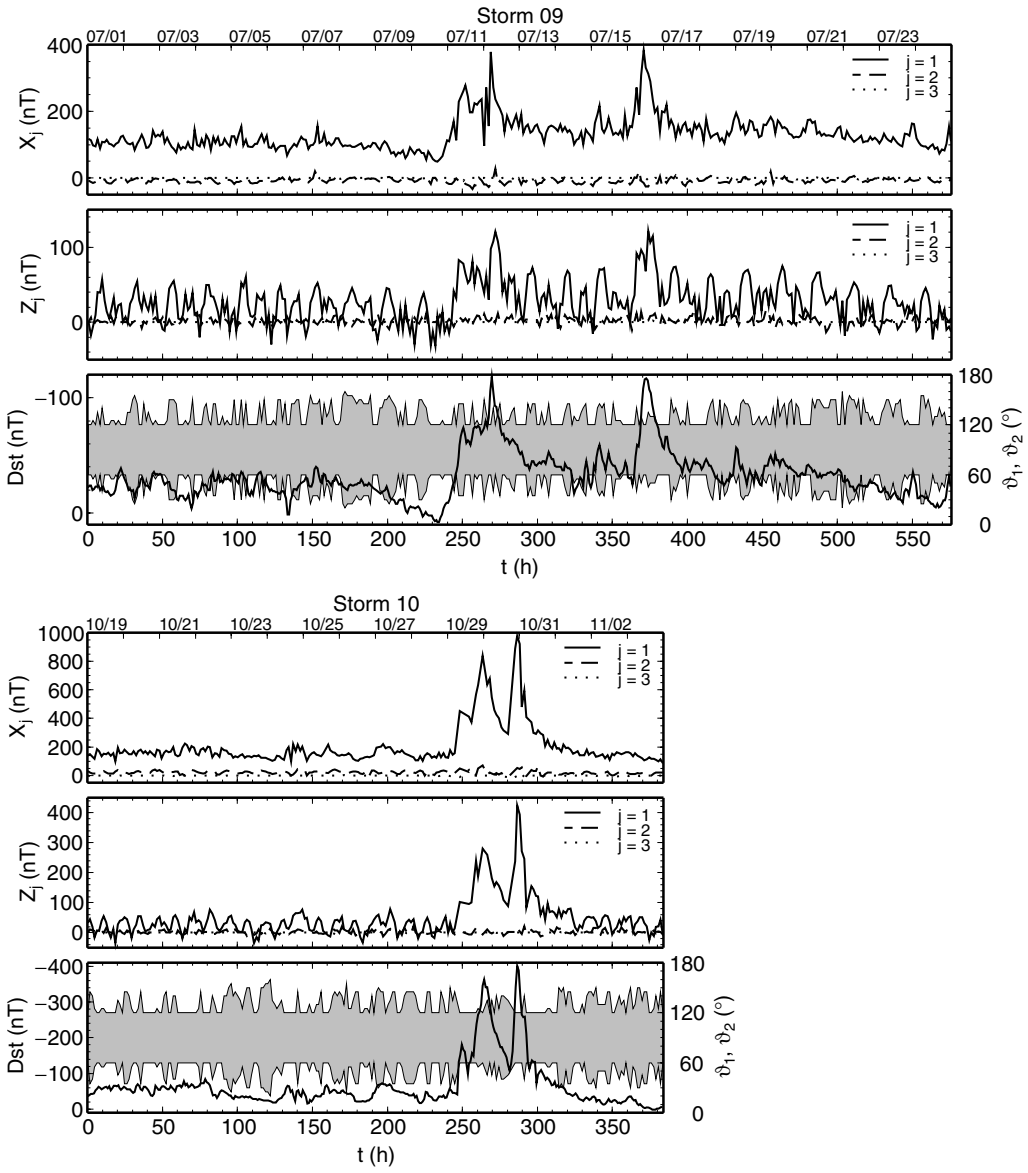

Figure 2. (*Continued*.)

the removal of ionospheric field there is still considerable signal at those periods from the magnetosphere.

The second remarkable point is the presence of peaks of the second and third degree coefficients, respectively, at frequencies 1 and 2 cpd. In order to explain these it is useful to convert the time-series of horizontal and vertical spherical harmonic coefficients X_j^i, Z_j^i into time-series of spherical harmonic components of external and internal field, $G_j^{(e),i}$ and $G_j^{(i),i}$. Comparing eqs (1) and (3) with Gaussian expansion of magnetic potential evaluated at radius b (Velímský & Martinec 2005) yields,

$$X_j^i = -\left[G_j^{(e),i} + G_j^{(i),i}\right], \tag{14}$$

$$Z_j^i = -\left[j\, G_j^{(e),i} - (j+1)\, G_j^{(i),i}\right], \tag{15}$$

which leads directly to evaluation of $G_j^{(e),i}$ and $G_j^{(i),i}$. Their ME power spectra estimates are shown in bottom plates of Fig. 3. One can see that the spectra of external field coefficients $G_2^{(e)}$ and $G_3^{(e)}$ also peak at respective frequencies of 1 and 2 cpd. Therefore, at least part of this signal must originate in the magnetosphere. They might be related to the fact the we attempt to express the magnetospheric field in the dipolar coordinate system which rotates with the Earth while the axial symmetry might be better expressed in coordinates related to the position of Sun (Maus & Lühr 2005). However, influence of some ionospheric contribution not removed by the Comprehensive Model cannot be ruled out as suggested by the large value of $G_2^{(i)}$ at 1 cpd.

4 1-D INVERSION

4.1 Evaluation of misfit in vertical component

In this section we present results of the inversion of the spherical harmonic time-series in terms of layered 1-D earth conductivity models. Each conductivity model is appraised by the misfit of its predicted Z response to the satellite observed vertical component.

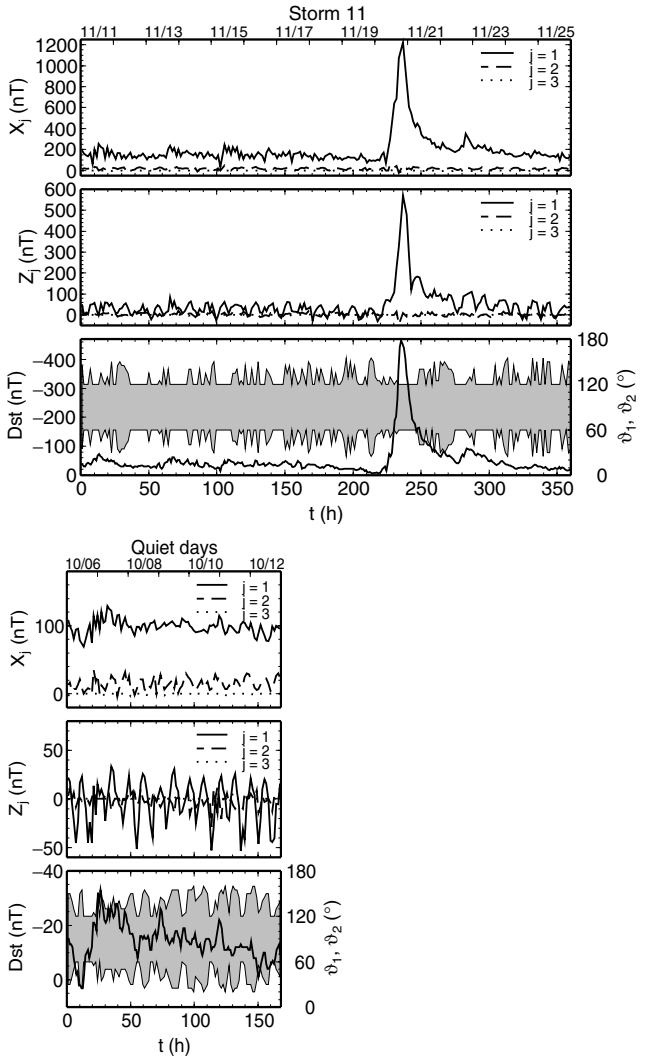

Figure 2. (*Continued*.)

Generally speaking, the spherical harmonic analysis of this component is not necessary to perform since the differences between observed and predicted Z data could be evaluated directly along the satellite tracks. However, since the forward approach yields the vertical component in terms of spherical harmonic coefficients, this method would require to synthesize the field for each conductivity model at each sampling point and along each track. This is avoided by expressing the misfit directly in the spherical harmonic domain. Moreover, the latter method reduces the effect of small-scale variations in the data which are beyond the resolution of our approach. Therefore, we define the misfit as

$$\chi^2(\boldsymbol{\sigma}; I) = \frac{1}{N_I} \sum_{i \in I} \sum_{j=1}^{N_Z^i} \left| Z_j^i - Z_j^i(\boldsymbol{\sigma}) \right|^2 , \tag{16}$$

where I is a particular selection of N_I tracks and $Z_j^i(\boldsymbol{\sigma})$ stands for spherical harmonic coefficients of the vertical component as predicted by forward modelling using conductivity model $\boldsymbol{\sigma}$. Since we use fully normalized spherical harmonic functions, no weighting of the misfit functional with respect to spherical harmonic degree j is introduced. The conductivity model $\boldsymbol{\sigma}$ is described by layer conductivities and depths of layer interfaces,

$$\boldsymbol{\sigma} = \{\sigma_1, h_1, \sigma_2, h_2, \ldots\} . \tag{17}$$

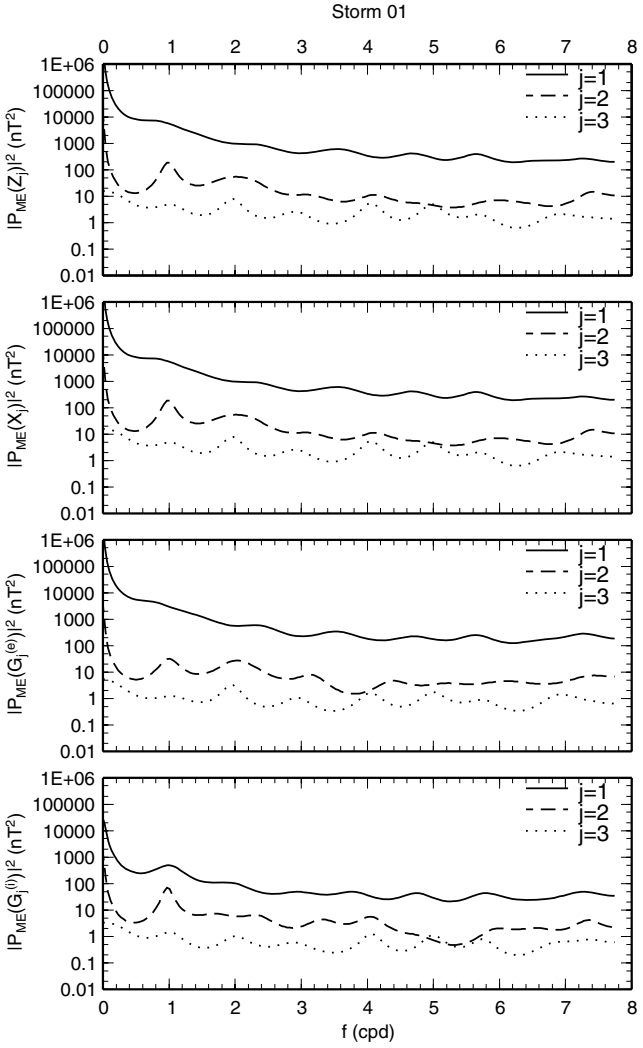

Figure 3. Power spectra estimates of spherical harmonic coefficients of vertical, horizontal, external and internal (top to bottom) field for Storm 1. Degrees of 1, 2 and 3 are, respectively, plotted by solid, dashed, and dotted lines.

The time integration of the forward modelling for each event is started from zero initial condition. Therefore, tracks from the first few days from each event are excluded from the misfit to avoid bias by the switch-on effect. That leaves $N_I = 1587$ tracks included in the misfit evaluation (16). The exact time needed to minimize the switch-on effect is determined individually for each storm based on data availability and is at least 6 days. Sufficiency of such a choice is easily checked by comparing forward solutions with different starting times (see Fig. 4). More details about the influence of zero initial condition on transient EM induction can be found in Velímský & Martinec (2005).

The novel time-domain forward technique is fast enough that it is tractable to explore the low-dimensional parametric space $\Sigma = \{\boldsymbol{\sigma}\}$ by systematic search. This allows us not only to find the best conductivity model within the model-space discretization limits but also to study the sensitivity of the misfit to variations in layer thicknesses and conductivities. In all results presented here we sample the conductivities on a log scale in 0.4 increments and interface depths in increments of 50 km. We consider three different parametrizations of model space Σ.

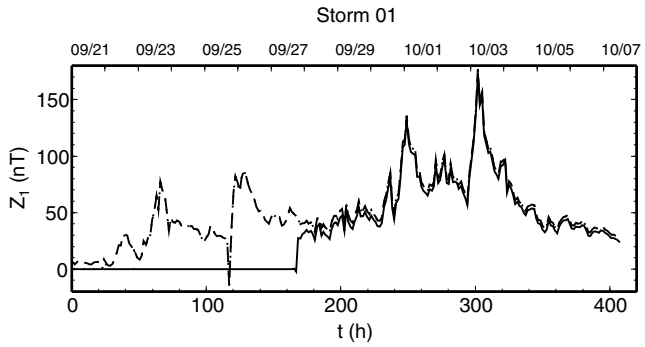

Figure 4. Influence of the initial value on forward modelling. Coefficients Z_1 computed for Storm 1 and three-layer conductivity model from Fig. 7 starting from zero initial value $t = 0$ (dashed), 24 (dotted) and 192 hr (solid line). Note that while the first two lines coincide, the results corresponding to the latest starting time differ during the actual storm.

4.2 Inversions in terms of layered models

First we interpret the satellite data in terms of a four-layer model. By placing interfaces at fixed depths of 50, 440 and 670 km, the model consists of crust, upper mantle, transition zone, and lower mantle. A conductive core ($\sigma_5 = 10^6$ S m^{-1}) is always assumed below 2891 km. All 11 storm events from Table 1 are used in the evaluation of the misfit. Fig. 5 shows the misfit χ^2 across six cross-sections of the 4-D parametric space. All cross-sections intersect the model which generates the minimum of the misfit function. Plates 1-1 to 1-3 (we refer to single plates in row-column coordinates, 1-1 being the upper left plate) indicate that the crust conductivity σ_1 is well resolved at 0.1 S m^{-1}. This value compares well with a global average of surface conductance (Everett *et al.* 2003) based on bathymetry, sediment thickness, and estimates of conductivity of water, crystalline rocks and sediments. Averaging the global conductance map over the Earth's surface yields 8000 S which corresponds to conductivity 0.16 S m^{-1} assuming a 50-km-thick layer.

Plates 1-3, 2-2 and 2-3 indicate that the lower mantle conductivity σ_4 is also well resolved at 6 S m^{-1}. This result is only slightly larger than the lower mantle conductivity inferred from surface observations, for example, European regional model by Olsen (1998), (1.7 S m^{-1} below 800 km) or Pacific semi-global model by Utada *et al.* (2003) (1.6 S m^{-1} below 850 km).

The inversion yields remarkably low conductivities ($\sigma_2, \sigma_3 \sim 10^{-2}$ to 10^{-4}] S m^{-1}) in the upper mantle (plates 1-1, 2-1, 2-2) and in the transition zone (plates 1-2, 2-1, 2-3). However, these values are not as well resolved as those in the crust and lower mantle. The L-shape of the misfit function in plate 1-1 allows an increase of σ_2 by more than one order of magnitude with a small reduction of crustal conductivity σ_1 without a significant increase of misfit. Mutual resolution between σ_2 and σ_3 is poor as indicated by a wide plateau of the misfit function in plate 2-1.

In the next configuration we use a three-layer conductivity model with a variable depth of the upper/lower mantle interface h_2. Its actual position is found by the inversion. The results of inverse modelling are shown in Fig. 6. Plates 2-1, 2-2 and 2-3 show that the depth of the interface h_2 is well resolved at 1020 km. The extreme value of σ_3 is several orders of magnitude larger than lower mantle conductivity estimates from previous EM induction studies (Olsen 1998; Utada *et al.* 2003) or laboratory measurements for perovskite (e.g. Xu *et al.* 1998). Note, however, that while h_2 is well constrained with respect to the conductivities of the resistive layers above, plate

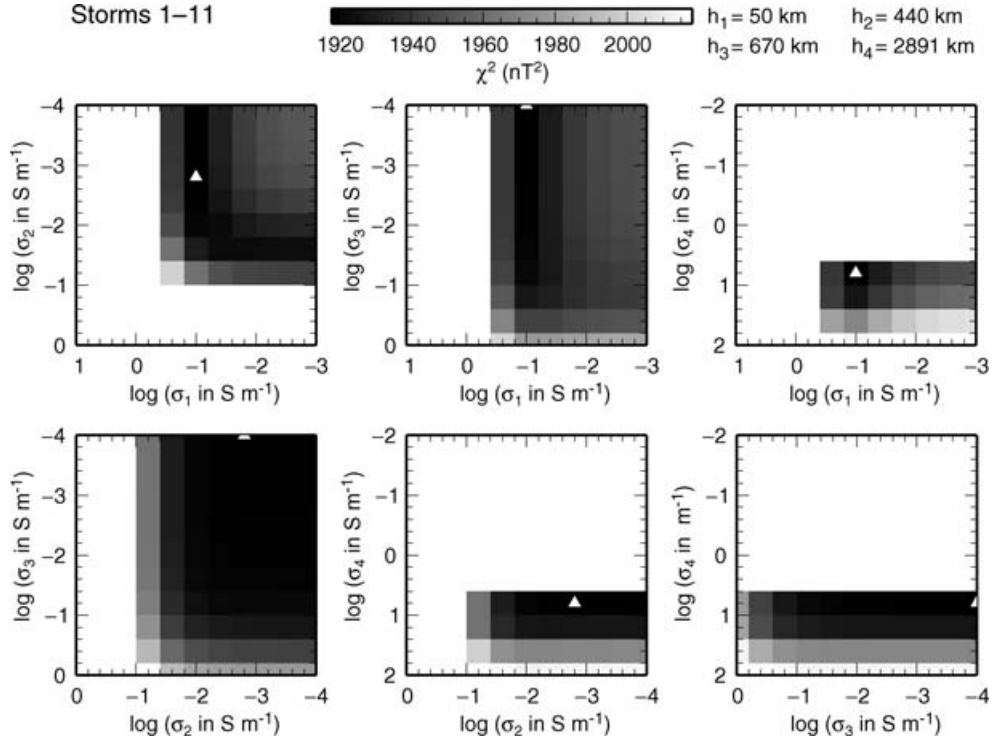

Figure 5. Results of 1-D inversion in terms of a four-layer model. The 4-D parametric space of crust, upper mantle, transition zone, and lower mantle conductivities σ_1, σ_2, σ_3, and σ_4 is systematically explored. Depths of interfaces h_1 to h_4 are fixed, respectively, at 50, 440, 670 and 2891 km and a highly conductive core ($\sigma_5 = 10^6$ S m^{-1}) is assumed. The best model with lowest χ^2 value is marked by white triangle. Plates show misfit χ^2 across various two-parametric cross-sections of the parametric space intersecting the best model.

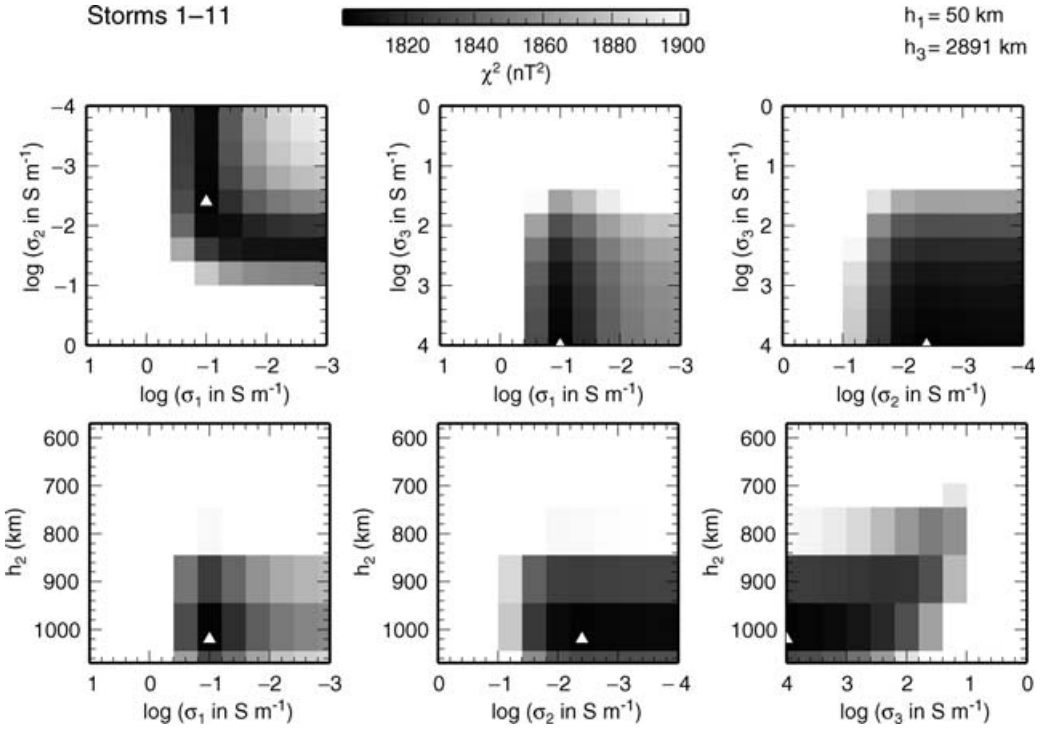

Figure 6. Results of 1-D inversion for a three-layer model. The 4-D parametric space of crust, upper mantle, and lower mantle conductivities σ_1, σ_2, σ_3 and depth of the upper/lower mantle interface h_2 is systematically explored. The depths of lithosphere/mantle and core/mantle interfaces h_1 and h_3 are fixed, respectively, at 50 and 2891 km and a highly conductive core ($\sigma_4 = 10^6$ S m^{-1}) is assumed.

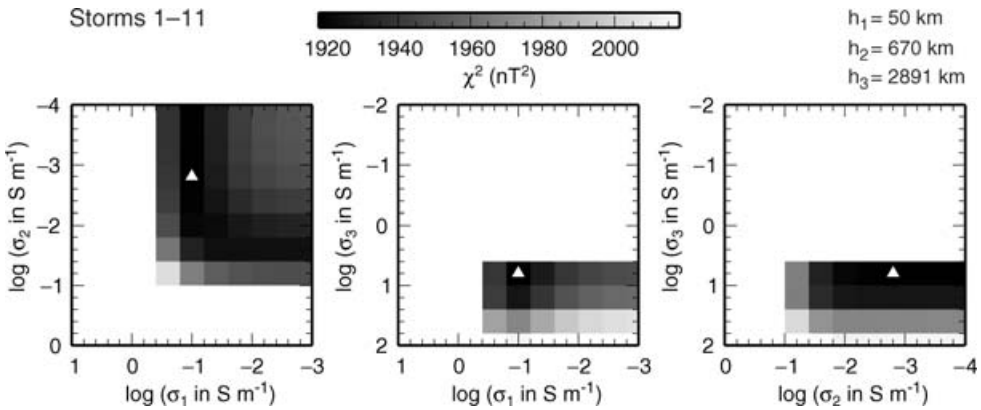

Figure 7. Results of 1-D inversion for a three-layer model. 3-D parametric space of crust, upper mantle, and lower mantle conductivities σ_1, σ_2, σ_3 is systematically explored. The depths of interfaces h_1, h_2 and h_3 are fixed, respectively, at 50, 670 and 2891 km and a highly conductive core ($\sigma_4 = 10^6$ S m^{-1}) is assumed.

2-3 allows a simultaneous reduction of h_2 and σ_3 by following the valley in the misfit surface.

By fixing the position of the upper/lower mantle interface h_2 at 670 km. we obtain the final three-layer model, shown in Fig. 7. The best model still favours a resistive upper mantle and conductive lower mantle. However, the achieved misfit is significantly larger than in the model with arbitrary position of the mantle interface.

4.3 Tests of robustness

Here we check the robustness of the results with respect to the choice of the events in the inversion. Table 2 shows the misfits of the best models from the three parametrizations described above evaluated separately for each storm. The misfits vary considerably with a distinct maximum corresponding to Storm 3. We investigate the influence of the variations on the results by solving the inverse problem separately for two different storm data sets. In Figs 8 and 9 we present the results of the three-layer inversion with mantle interface fixed at 670 km, as described above, using data sets comprising, respectively, of odd-numbered and even-numbered storm events from Table 1. This is done to determine whether the inversion is biased by the particular set of storms we analysed. The misfit is evaluated over $N_I^{\text{odd}} = 830$ and $N_I^{\text{even}} = 757$ tracks, respectively.

These results confirm the facts that (i) the crust and lower mantle conductivity are determined robustly and similar values are required by both data sets, (ii) in the upper mantle conductivity is constrained only weakly, since different data sets allow for differences of more

Table 2. Misfit of the best models evaluated separately for storms 1–11. The three columns correspond, respectively, to the four-layer parametrization and three-layer parametrization with variable and fixed mantle interface. N_I is the number of tracks used for each storm and according to eq. (16) is applied as a weight in order to obtain the total misfit from all storms.

Storm	N_I	χ^2 (nT^2)		
1	139	1879.32	1811.73	1879.51
2	138	1124.21	992.16	1124.62
3	104	10337.02	10154.77	10337.17
4	182	1121.64	1091.93	1121.68
5	156	341.59	332.97	341.56
6	200	687.61	703.85	687.71
7	78	845.42	850.05	845.28
8	123	811.72	821.49	811.62
9	248	1579.49	1364.87	1579.26
10	114	2625.19	2359.02	2625.20
11	105	2870.17	2391.58	2870.45
All	1587	1918.40	1803.51	1918.45

than one order of magnitude (compare plates 1-1 in Figs 8 and 9). Obviously, the best model found previously by inversion of all data (Fig. 7) is a compromise between the best models found for both subsets. Runs based on other selections of storms (e.g. using all storms except No. 3) which are not shown here yield same conclusions.

In the following test we evaluate by means of forward modelling the synthetic time-series of Z_j^i coefficients using the original CHAMP-derived X_j^i series and the best three-layer model from Fig. 7. Then we solve the inverse problem with synthetic data in place of the Z_j^i based on CHAMP measurements. Fig. 10 shows not only full recovery of the best model but also remarkable similarity of the shape of the misfit function in the parametric space, albeit on a much reduced scale. Adding a 10 nT Gaussian noise to the synthetic Z_j^i series prior inversion yields similar results (Fig. 11). The lower-mantle conductivity σ_3 is recovered accurately, crust and upper mantle values are affected by the noise.

Finally, Fig. 12 shows results of the inversion based on data from the seven quiet days marked as '*Q*' in Table 1. Note that the magnetic field of ionospheric currents and corresponding induced currents has been removed from the data. Therefore, apart from noise and inaccuracies in the comprehensive model, these data represent only quiet-time variations of ring currents. Plates 1-1 and 1-2 show that, without storm-time excitation, the time-domain method is definitely insensitive to mantle conductivity. The model with the lowest misfit actually lies at the boundaries of the explored part of parametric space. We do not, however, extend the parametric space since we prefer to keep the parameter range within reasonable values and consistent with previous runs.

5 CONCLUSIONS

The numerical results of this study prove the feasibility of time-domain approach to the EM induction (Martinec & McCreadie 2004) to interpret satellite data in terms of the Earth's conductivity structure. The inversion of quiet-time data showed almost no resolution to mantle conductivity, lending confidence to the underlying supposition that storm-time data are sensitive to deep earth electrical structure by virtue of the powerful electromotive force engendered by rapid time changes of the ring current system.

Inversion results for the different parametrizations are summarized in Fig. 13. For each parametrization the figure shows the best model as well as models with misfit χ^2 within 0.2 per cent from the minimum. Such a small value is chosen because of the extreme flatness of the misfit functions near their global minima. The models accommodating the seismic-based 670 km interface yield robust estimates of conductivity about 6 S m^{-1} in the lower mantle. However, the model with an adjustable interface in the lower mantle suggests a large increase of conductivity to at least 10^3 S m^{-1} around 1000 km. The existence of such a jump in the models is supported by a significant reduction of the misfit. Note, however, that the inverse modelling used here does not implement any additional constraints on the smoothness of conductivity models.

The conductivity of the crust represented by a uniform layer 50 km thick is estimated at 0.1 S m^{-1}, a value consistent with the global average of the independently derived surface conductance map (Everett *et al.* 2003).

The upper mantle may be thought as a resistor embedded between two conductors. This explains why its conductivity is poorly resolved. Our results confirm that the upper mantle conductivity does not exceed 0.01 S m^{-1} and some models even admit values two orders of magnitude smaller. Moreover the four-layer model does not suggest any conductivity increase in the transition zone.

Inverse modelling for two separate storm-time data subsets results in different conductivities in the upper mantle. Since the geographic footprint of the satellite around peak times of the storms is generally different in both data sets, the poor resolution of upper mantle might also be caused by lateral conductivity heterogeneities. Satellite data could be biased towards different mantle regions depending on the

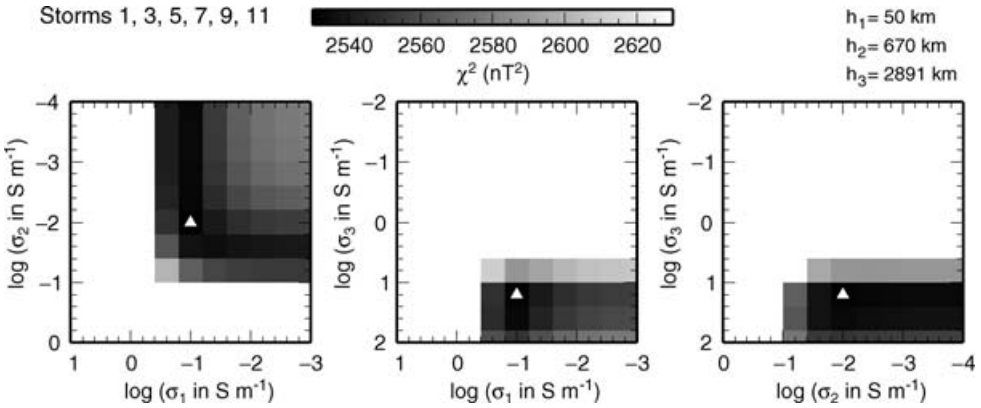

Figure 8. Test of robustness of the inversion. Only odd-numbered storms from Table 1, containing approximately half of the tracks, are used in the inversion. Conductivity parametrization is the same as in Fig. 7.

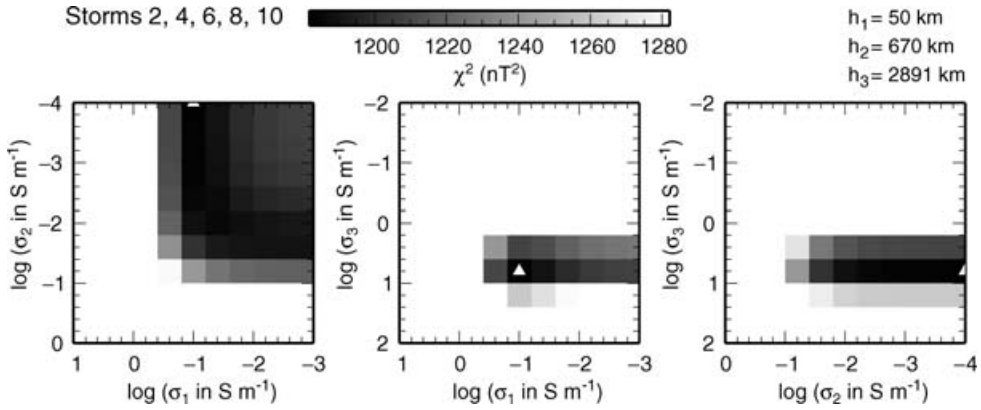

Figure 9. Test of robustness of the inversion. Only even-numbered storms from Table 1, containing approximately half of the tracks, are used in the inversion. Conductivity parametrization is the same as in Fig. 7.

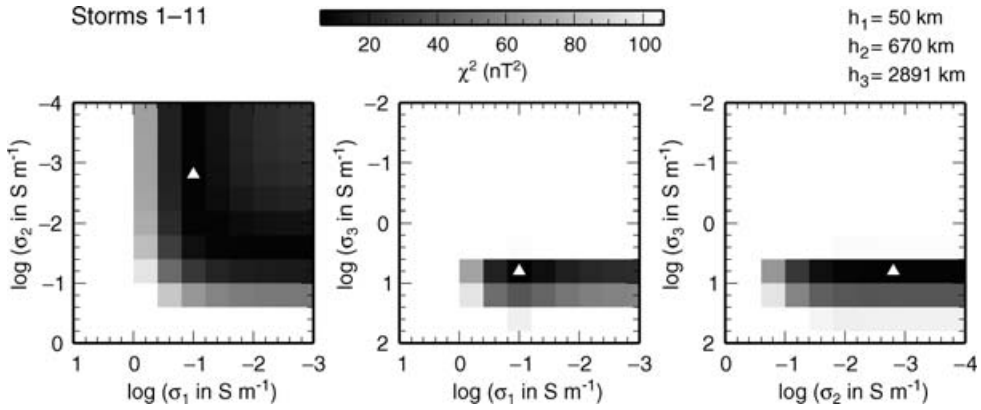

Figure 10. Test of robustness of the inversion. Synthetic Z_j^i series corresponding to the best model in Fig. 7 are fed back into the inversion scheme using identical parametrization and the model is recovered.

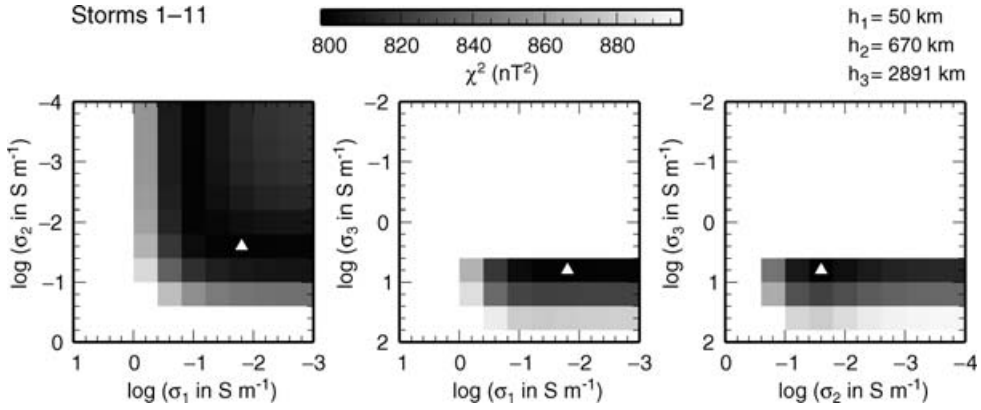

Figure 11. Test of robustness of the inversion, similar to Fig. 10. Gaussian noise with 10 nT standard deviation is added to the synthetic Z_j^i series prior inversion.

satellite geographical position. This hypothesis is being investigated with 2-D and 3-D modelling.

ACKNOWLEDGMENTS

We thank the staff of the *CHAMP Information System and Data Center* which provided us with access to the vector magnetometer data. The comprehensive model subroutines and coefficients were made available by T. Sabaka. Helpful comments from K. Bahr, Y. Hamano and A. V. Kuvshinov are much appreciated. JV would like to thank Texas A& M Harris Postdoctoral Fellowship program and the 1K05003 program of the Ministry of Education, Youth and Sports of the Czech Republic for support. The research presented in this paper was partly supported by the Grant Agency of the Czech Republic through Grants No. 205/03/1001 and 205/06/0557. Figures were prepared using GMT.

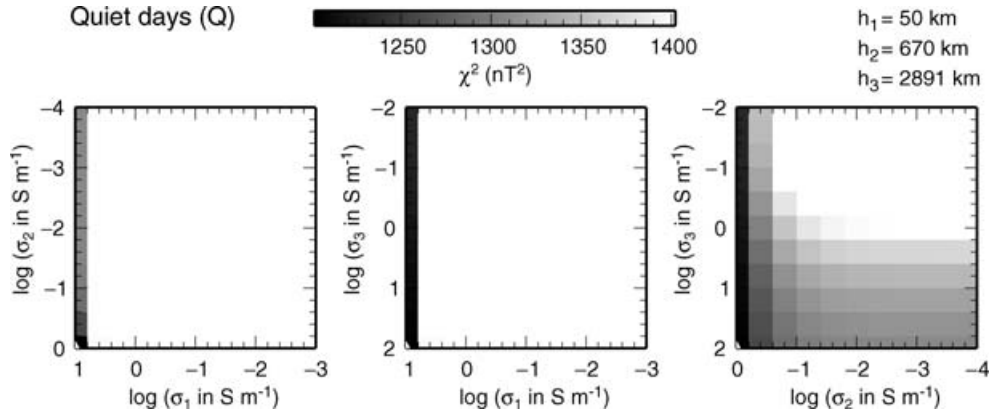

Figure 12. Test of event selection. Data from a series of quiet days are inverted in terms of three-layer model. Compare with Fig. 7.

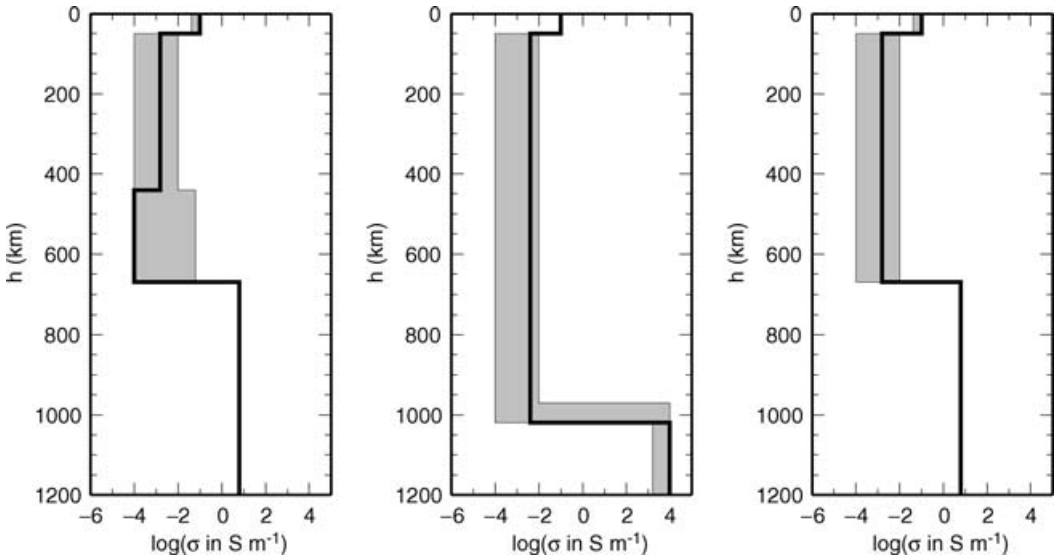

Figure 13. Summary of inversion results for, respectively, the four-layer model with fixed interface depths (left), the three-layer model with variable mantle interface depth and the three-layer model with all fixed interfaces (right). Solid lines show the best models, grey shadings show models with the misfit χ^2 within 0.2 per cent from the minimum for each particular parametrization.

REFERENCES

Balasis, G., Egbert, G.D. & Maus, S., 2004. Local time effects in satellite estimates of electromagnetic induction transfer functions, *Geophys. Res. Lett.,* **31,** L16610, doi:10.1029/2004GL020147.

Constable, S. & Constable, C., 2004. Observing geomagnetic induction in magnetic satellite measurements and associated implications for mantle conductivity, *Geochem. Geophys. Geosyst.,* **5,** Q01006, doi:10.1029/2003GC000634.

Davis, T.A. & Duff, I.S., 1999. A combined unifrontal/multifrontal method for unsymmetric sparse matrices, *ACM Transactions on Mathematical Software,* **25**(1), 1–19.

Everett, M.E. & Martinec, Z., 2003. Spatiotemporal response of a conducting sphere under simulated geomagnetic storm conditions, *Phys. Earth planet. Inter.,* **138,** 163–181.

Everett, M.E., Constable, S. & Constable, C., 2003. Effects of near-surface conductance on global satellite induction responses, *Geophys. J. Int.,* **153,** 277–286.

Hamano, Y., 2002. A new time-domain approach for the electromagnetic induction problem in a three-dimensional heterogeneous earth, *Geophys. J. Int.,* **150,** 753–769.

Kuvshinov, A.V., Sabaka, T. & Olsen, N., 2006. 3-D electromagnetic induction at *Swarm* constellation: Mapping the conductivity anomalies in the mantle, *Earth Planets Space* **58** (4), 417–427.

Martinec, Z. & McCreadie, H., 2004. Electromagnetic induction modeling based on satellite magnetic vector data, *Geophys. J. Int.,* **157,** 1045–1060.

Martinec, Z., Everett, M.E. & Velímský, J., 2003. Time-domain, spectral-finite element approach to transient two-dimensional geomagnetic induction in a spherical heterogeneous earth, *Geophys. J. Int.,* **155,** 33–43.

Maus, S. & Lühr, H., 2005. Signature of the quiet-time magnetospheric magnetic field and its electromagnetic induction in the rotating Earth, *Geophys. J. Int.,* **162,** 755–763.

Olsen, N., 1998. The electrical conductivity of the mantle beneath Europe derived from C-responses from 3 to 720 hr, *Geophys. J. Int.,* **133,** 298–308.

Olsen, N., 1999. Induction studies with satellite data, *Surveys in Geophysics,* **20,** 309–340.

Olsen, N. & Kuvshinov, A.V., 2004. Modelling the ocean effect of geomagnetic storms., *Earth Planets Space,* **56,** 525–530.

Press, W.H., Teukolsky, S.A., Vetterling, W.T. & Flannery, B.P., 1992. *Numerical recipes in Fortran. The art of scientific computing*, Cambridge University Press, Cambridge.

Sabaka, T.J., Olsen, N. & Langel, R.A., 2002. A comprehensive model of the quiet-time, near-Earth magnetic field: phase 3, *Geophys. J. Int.,* **151,** 32–68.

Sabaka, T.J., Olsen, N. & Purucker, M.E., 2004. Extending comprehensive models of the Earth's magnetic field with Ørsted and CHAMP data, *Geophys. J. Int.,* **159,** 521–547.

Utada, H., Koyama, T., Shimizu, H. & Chave, A.D., 2003. A semi-global reference model for electrical conductivity in the mid-mantle beneath the north Pacific region, *Geophys. Res. Lett.,* **30**(4), 1194, doi:10.1029/2002GL016092.

Velímský, J., Everett, M.E. & Martinec, Z., 2003. The transient Dst electromagnetic induction signal at satellite altitudes for a realistic 3-D electrical conductivity in the crust and mantle, *Geophys. Res. Lett.,* **30**(7), 1355.

Velímský, J. & Martinec, Z., 2005. Time-domain, spherical harmonic-finite element approach to transient three-dimensional geomagnetic induction in a spherical heterogeneous Earth, *Geophys. J. Int.,* **161,** 81–101.

Xu, Y., McCammon, C. & Poe, B.T., 1998. The effect of alumina on the electrical conductivity of silicate perovskite. *Science,* **282,** 922–924.